Theoretical and Applied Mechanics Letters 12 (2022) 100352

Contents lists available at ScienceDirect

Theoretical and Applied Mechanics Letters

journal homepage: www.elsevier.com/locate/taml

Letter

Motion of a sphere and the suspending low-Reynolds-number fluid confined in a cubic cavity

Gaofeng Chen[a,b], Xikai Jiang[a,b,*]

[a] State Key Laboratory of Nonlinear Mechanics, Institute of Mechanics, Chinese Academy of Sciences, Beijing 100190, China
[b] School of Engineering Science, University of Chinese Academy of Sciences, Beijing 100049, China

ARTICLE INFO

Article history:
Received 28 May 2022
Accepted 13 June 2022
Available online 23 June 2022

Keywords:
Particle dynamics
Low-Reynolds-number fluid
Confinement
Mobility
Drift

ABSTRACT

Dynamics of a spherical particle and the suspending low-Reynolds-number fluid confined by a cubic cavity were studied numerically. We calculated the particle's hydrodynamic mobilities along *x*-, *y*-, and *z*-directions at various locations in the cavity. The mobility is largest in the cavity center and decays as the particle becomes closer to no-slip walls. It was found that mobilities in the entire cubic cavity can be determined by a minimal set in a unit tetrahedron therein. Fluid vortices in the cavity induced by the particle motion were observed and analyzed. We also found that the particle can exhibit a drift motion perpendicular to the external force. Magnitude of the drift velocity normalized by the velocity along the direction of the external force depends on particle location and particle-to-cavity sizes ratio. This work forms the basis to understand more complex dynamics in microfluidic applications such as intracellular transport and encapsulation technologies.

© 2022 The Author(s). Published by Elsevier Ltd on behalf of The Chinese Society of Theoretical and Applied Mechanics.
This is an open access article under the CC BY-NC-ND license (http://creativecommons.org/licenses/by-nc-nd/4.0/)

Particulate transport in the low-Reynolds-number fluid under confinement finds a wide variety of applications ranging from particle manipulation in lab-on-a-chip devices to macromolecular transport in biological tissues [1–3]. Recently, particle dynamics under total confinement have drawn much attention because it is important to microfluidic encapsulation techonologies and biological functions in living cells [4–9]. In cells, biological particles in the cytoplasmic fluid are confined by the cell membrane, and their confined motion can affect intracellular activities such as cellular homeostasis, signaling, and metabolism [10,11]. Experimental studies have revealed intriguing transport phenomena in the cytoplasm such as cytoplasmic streaming and hindered diffusion of proteins [9,12]. To understand mechanisms behind these phenomena, numerical and theoretical studies have been carried out over the past decades. In these modeling works, the cytoplasm was treated as a continuum fluid confined in a cavity [13,14]. Through Brownian and Stokesian dynamics simulations, effects of crowding, hydrodynamic and steric interactions, and confinement were found to play vital roles in active and passive motion of intracellular particles [4,5,7,8,15].

Single-particle dynamics in the low-Reynolds-number fluid under total confinement is also important, as it forms the basis to understand more complex dynamics in concentrated suspensions. In most prior studies, particles were considered to be confined in a spherical cavity, mainly because the shapes of many cells and droplet-based microreactors are spherical and this geometry makes it simple for analyzing results while revealing key features of intracellular transport [8,16–19]. However, less attention have been paid on cavities with other shapes. One of the shapes is the cube, which can be found in plant cells, cuboidal epithelium, and microcapsules for drug delivery systems [20–22]. In a prior study, dynamics of a spherical and an ellipsoidal particle in a low-Reynolds-number fluid confined by a cubic cavity were examined by boundary element method. The particles' friction coefficients at the cavity center and their settling translational and angular velocities at different locations in the cavity were calculated [23]. Despite these progress, hydrodynamic mobilities of the particle at other locations in the cubic cavity, the particle's drift motion perpendicular to the external force, and distributions of fluid velocities in the cavity remain to be explored. In this work, we address these issues by numerical simulations.

We consider a rigid spherical particle in a quiescent low-Reynolds-number fluid confined by a cubic cavity. The schematic of the simulation system is shown in Fig. 1a. The radius of the

* Corresponding author.
E-mail address: xikaij@imech.ac.cn (X. Jiang).

https://doi.org/10.1016/j.taml.2022.100352
2095-0349/© 2022 The Author(s). Published by Elsevier Ltd on behalf of The Chinese Society of Theoretical and Applied Mechanics. This is an open access article under the CC BY-NC-ND license (http://creativecommons.org/licenses/by-nc-nd/4.0/)

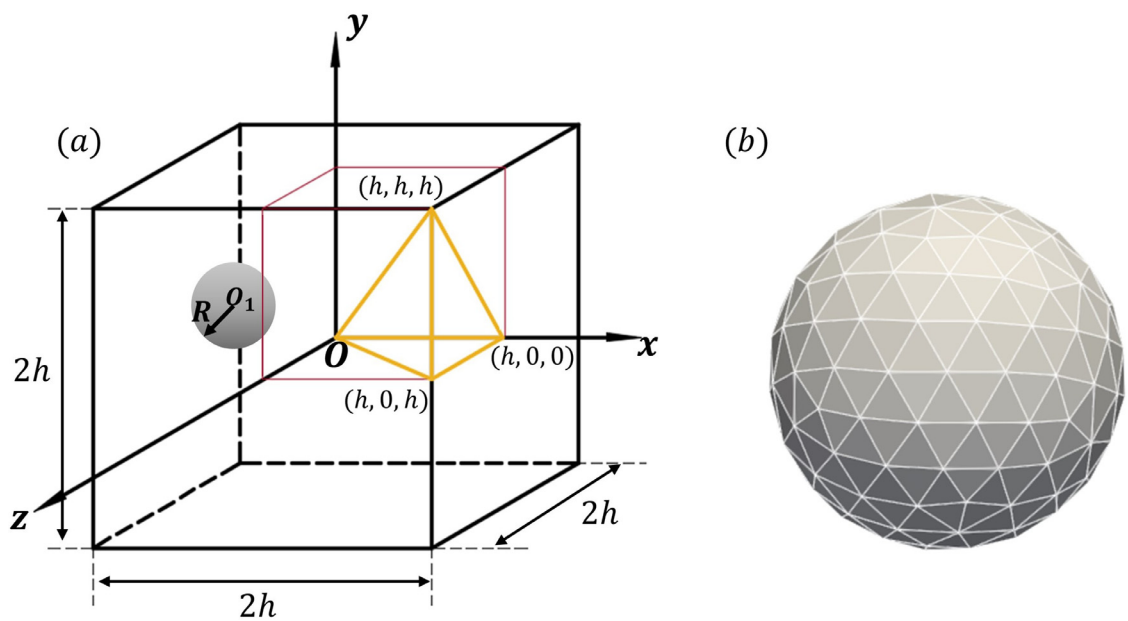

Fig. 1. (**a**) Schematic of the simulation system for studying dynamics of a spherical particle and the suspending low-Reynolds-number fluid confined by a cubic cavity; (**b**) Discretization of the spherical particle.

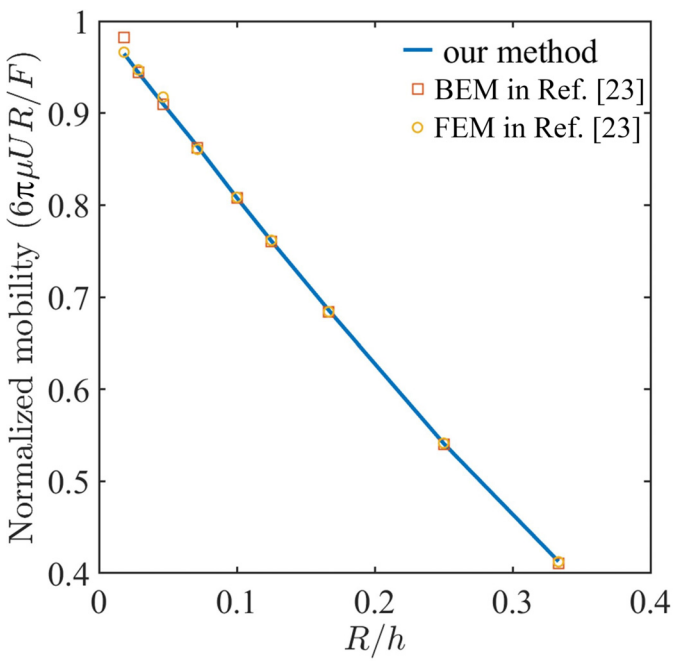

Fig. 2. Normalized mobility of the spherical particle along *x*-, *y*-, or *z*-direction at the cavity center plotted against particle-to-cavity sizes ratio R/h. Blue line is our numerical result. Squares (circles) are results from boundary (finite) element method in Ref. [23].

spherical particle is R, and the side length of the cubic cavity is $2h$. Cartesian coordinate system is used in this study, and the origin (0, 0, 0) is the cavity center. Neglecting inertial effects and Brownian motion, the balance equation for force and torque on the particles is

$$\boldsymbol{F}^H + \boldsymbol{F}^{ext} = \boldsymbol{0}, \tag{1}$$

where $\boldsymbol{F}^H$ is the hydrodynamic force/torque vector and $\boldsymbol{F}^{ext}$ contains external forces/torques. In our numerical method, the particle surface is discretized into a set of N nodes. Each node is connected with its neighbouring nodes by elastic springs with a large spring constant, in order to model the rigid particle and maintain particle shape. The nodes are also connected with the particle center-of-mass by stiff springs to avoid particle deformation [24]. Discretization of the spherical particle is shown in Fig. 1b. Equation (1) is then translated into the N surface nodes as

$$\boldsymbol{f}_i^H + \boldsymbol{f}_i^S + \boldsymbol{f}_i^{ext} = \boldsymbol{0}. \tag{2}$$

here, $i = 1, 2, \ldots, N$, $\boldsymbol{f}_i^H$ is the hydrodynamic force, $\boldsymbol{f}_i^S$ is the spring force, and $\boldsymbol{f}_i^{ext}$ are external forces. The spring force acting on the ith node by the jth node is

$$\boldsymbol{f}_{ij}^S = k\left(|\boldsymbol{r}_{ij}| - r_0\right)\frac{\boldsymbol{r}_{ij}}{|\boldsymbol{r}_{ij}|}, \tag{3}$$

where k is the spring constant, r_0 is the equilibrium spring length for each spring, $\boldsymbol{r}_{ij} = \boldsymbol{r}_i - \boldsymbol{r}_j$, and $\boldsymbol{r}_i$ and $\boldsymbol{r}_j$ are coordinates of the ith and jth nodes. The external force on the ith node is $\boldsymbol{f}_i^{ext} = \boldsymbol{F}^{ext}/N$.

The equation of motion for all nodes on the particle surface is

$$\mathrm{d}\boldsymbol{R} = [\boldsymbol{U}_0 + \boldsymbol{M}\cdot\boldsymbol{F}]\mathrm{d}t, \tag{4}$$

where $\boldsymbol{R} = (\boldsymbol{r}_1, \boldsymbol{r}_2, \ldots, \boldsymbol{r}_N)$ denotes a $3N$ vector containing nodal coordinates, $\boldsymbol{U}_0$ denotes a $3N$ vector with the undisturbed fluid velocity at nodal positions, and $\boldsymbol{M}$ is the $3N \times 3N$ mobility tensor. $\boldsymbol{U} = (\boldsymbol{u}_1, \boldsymbol{u}_2, \ldots, \boldsymbol{u}_N) = \boldsymbol{M}\cdot\boldsymbol{F}$ contains $3N$ disturbed velocities from the hydrodynamic interaction (HI), and $\boldsymbol{F} = (\boldsymbol{f}_1, \boldsymbol{f}_2, \ldots, \boldsymbol{f}_N)$ is a $3N$ vector including non-HI forces on the surface nodes. The translational and rotational motion of the rigid particle are realized by integrating Eq. (4) for all surface nodes, satisfying the balance equation for force and torque. The velocity field $\boldsymbol{U}$ driven by nodal forces $\boldsymbol{F}$ can be obtained by solving the Stokes equation

$$-\nabla p + \mu\nabla^2\boldsymbol{u} = -\boldsymbol{f}, \quad \nabla\cdot\boldsymbol{u} = 0, \tag{5}$$

where p is the fluid pressure, μ is the fluid viscosity, $\boldsymbol{u}$ is the fluid velocity, and $\boldsymbol{f}(\boldsymbol{r}) = \sum_{i=1}^{N}\boldsymbol{f}_i(\boldsymbol{r}_i)\delta(\boldsymbol{r} - \boldsymbol{r}_i)$ is the force density exerting on the fluid. To avoid singularity due to point forces placed at nodes on the particle surface, the smoothing function $\delta(\boldsymbol{r})$ is used to regularize the point forces, and it takes the form of a modified Gaussian function

$$\delta(\boldsymbol{r}) = \frac{\xi^3}{\pi^{3/2}}\mathrm{e}^{-\xi^2|\boldsymbol{r}|^2}\left(\frac{5}{2} - \xi^2|\boldsymbol{r}|^2\right). \tag{6}$$

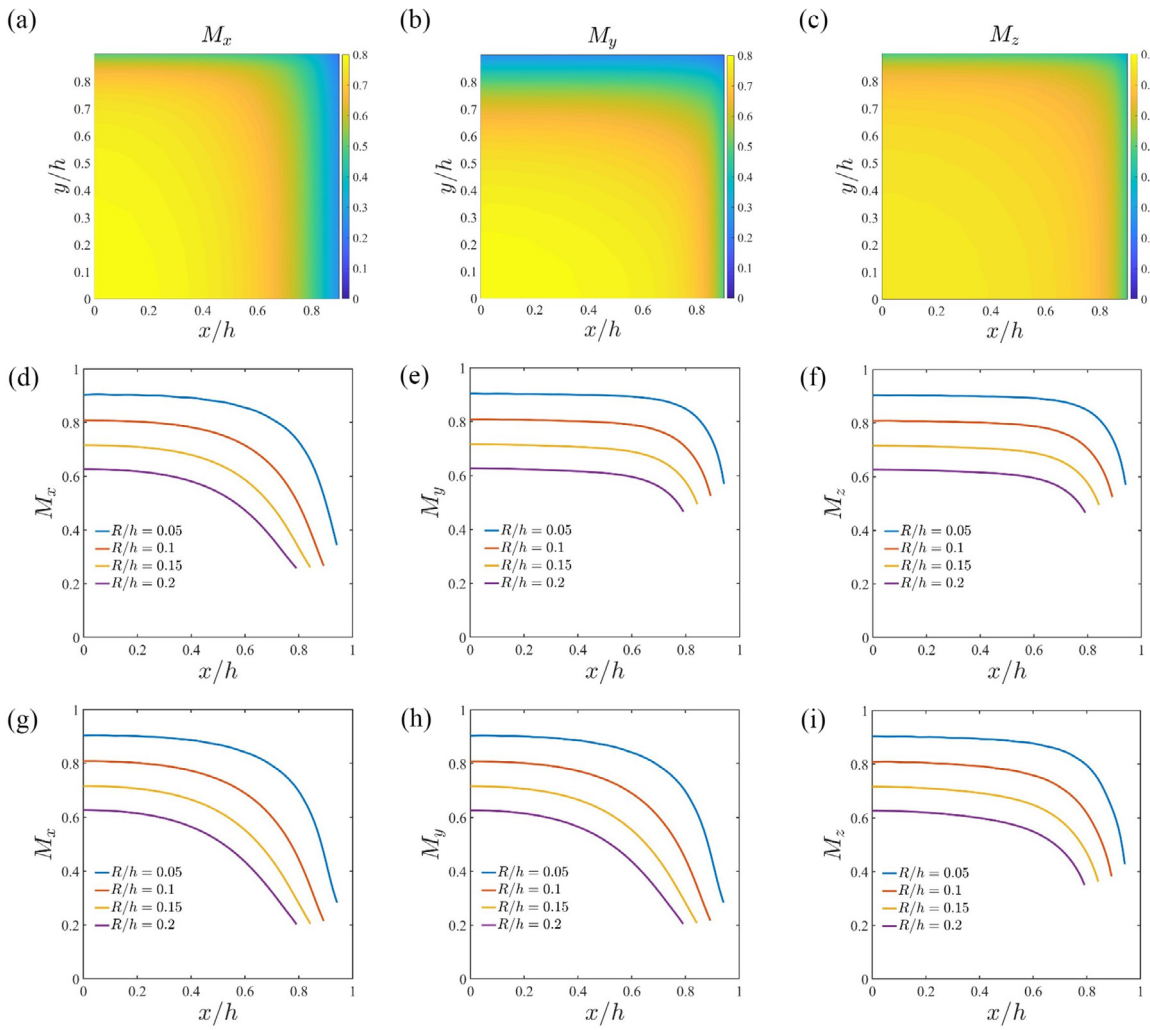

Fig. 3. (**a**-**c**) Two-dimensional distributions of M_x, M_y, and M_z for a particle with $R/h = 0.1$ in the plane defined by $0 \le x/h \le 1$, $0 \le y/h \le 1$, and $z = 0$. (**d**-**f**) M_x, M_y, and M_z under different R/h versus scaled particle x-position along the line defined by $0 \le x/h \le 1$ and $y = z = 0$. (**g**-**i**) M_x, M_y, and M_z under different R/h versus scaled particle x-position along the line defined by $0 \le x/h \le 1$, $x = y$, and $z = 0$. (For interpretation of the references to color in this figure legend, the reader is referred to the web version of this article.)

The regularization parameter ξ is related to the characteristic node spacing on the particle surface h, i.e., $\xi \sim h^{-1}$. This is to ensure that the regularized force density is spread over the length scale of associated surface elements on the particle, preventing the fluid from penetrating the particle surface [5,25,26]. For the undisturbed fluid velocity in Eq. (4), we set $\boldsymbol{U}_0 = \boldsymbol{0}$ to model the quiescent fluid. No-slip boundary condition is applied on all walls of the cavity.

The aforementioned equations for particle dynamics and fluid motion are solved using the General Geometry Ewald-like Method. Details of the method can be found in Ref. [24]. The method has been validated for the sedimentation of a spherical particle between two parallel walls [5]. It has also been used to study collision and segregation behavior of fluid-filled elastic capsules in confined simple shear flows [25,27]. In the remainder of this work, we will first validate the method against numerical solutions for the hydrodynamic mobility of a spherical particle at the center of the cubic cavity; we will then apply it to study dynamics of the particle and the suspending fluid under cubic confinement. Dimensionless variables are used in this study, and they are based on a set of characteristic scales. The characteristic length scale is l (hydrodynamic radius of each node), the energy scale is k_BT where k_B is Boltzmann constant and T is temperature, and the force scale is k_BT/l.

We first calculate hydrodynamic mobility of the spherical particle at the cavity center normalized by that of the same particle in unbounded fluid. Due to the symmetry of the cubic cavity, normalized mobilities along x-, y-, and z-directions (M_x, M_y, M_z) are the same at the cavity center. Results for one of the mobilities under various particle-to-cavity sizes ratios (R/h) are shown in Fig. 2. As R/h increases (particle size increases or cavity size decreases), normalized mobility of the particle decreases due to increased level of confinement and greater influence of no-slip walls on the particle. Results from Ref. [23] are also included in Fig. 2, and our numerical results agree well with those reported in the literature.

We then calculate M_x, M_y, and M_z of a particle with $R/h = 0.1$ in a quarter of a midplane of the cubic cavity, which is defined by $0 \le x/h \le 1$, $0 \le y/h \le 1$, and $z = 0$. Due to the symmetry of the cubic geometry, mobilities at the other three quarters of the midplane can be determined by those in the selected one. Two-dimensional distributions of the mobilities in the chosen plane are shown in Fig. 3a–3c. It can be seen that, in general, the mobility is largest in the cavity center and decays as the particle becomes closer to no-slip walls. M_x and M_y are found to be symmetric about the diagonal of the chosen plane, while M_z itself is symmetric about the diagonal. We further select two lines in the plane and analyze variations of mobilities along them. The first

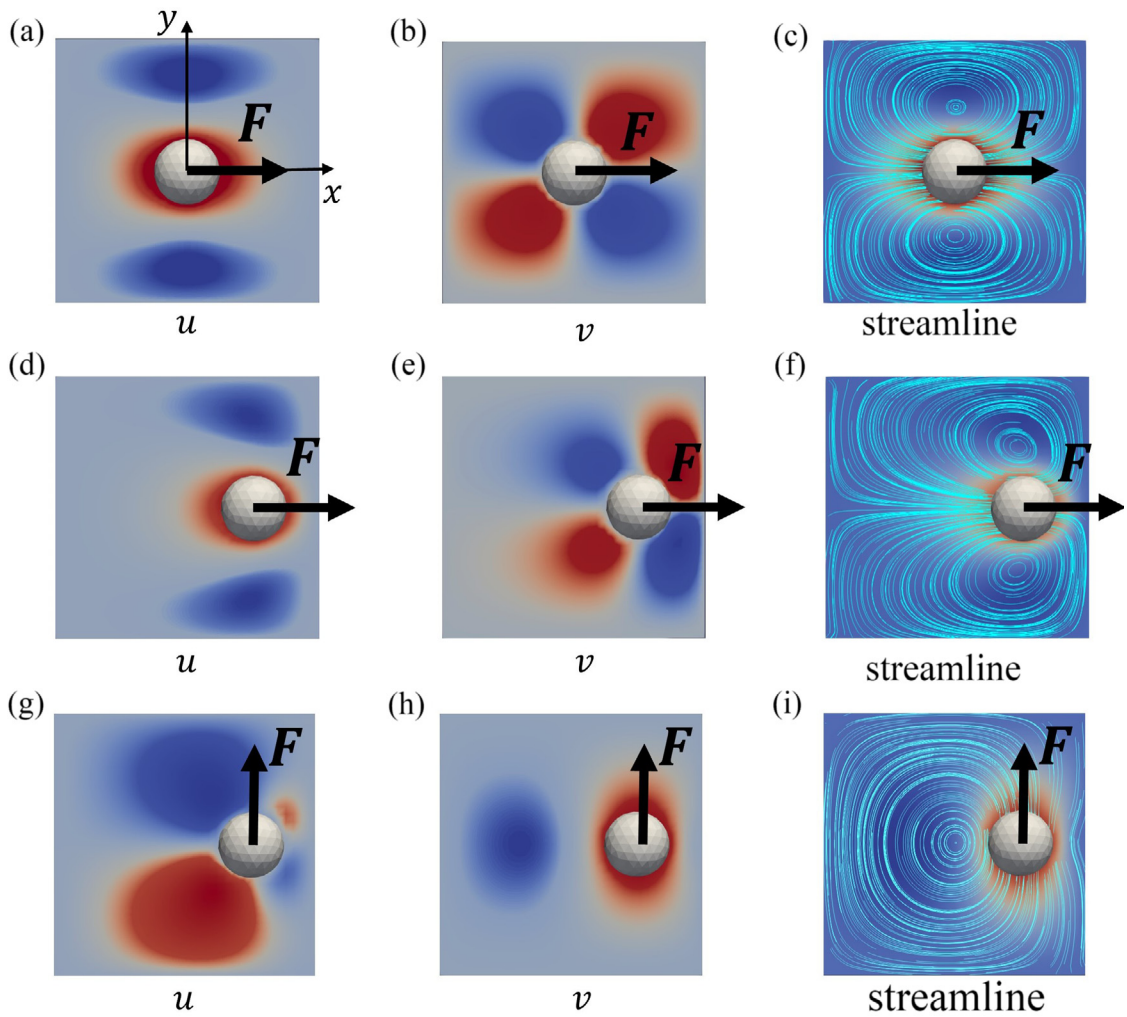

Fig. 4. Two-dimensional distributions of fluid velocity in x- and y-directions (u and v) and streamlines in the midplane of the cubic cavity at $z = 0$. Red (blue) color denotes positive (negative) value. (**a**-**c**) Particle center is at the origin and the external force ($\boldsymbol{F}$) is in positive x-direction. (**d**-**f**) Particle center is at (0.5h, 0, 0) and $\boldsymbol{F}$ is in positive x-direction. (**g**-**i**) Particle center is at (0.5h, 0, 0) and $\boldsymbol{F}$ is in positive y-direction. (For interpretation of the colors in this figure, the reader is referred to the web version of this article.)

line is defined by $0 \le x/h \le 1$ and $y = z = 0$, and relevant results are shown in Fig. 3d–3f; the second line is defined by $0 \le x/h \le 1$, $x = y$, and $z = 0$, and relevant results are shown in Fig. 3g–3i. In general, the mobility at a certain location decreases as R/h increases because the confinement level increases and the no-slip walls exert greater influence on the particle. On the first line, M_x is perpendicular to the wall at $x = h$, while M_y and M_z are parallel to this wall and $M_y = M_z$. Under a specific R/h, M_x is smaller than M_y (M_z) when the particle is between cavity center and cavity wall at $x = h$. As the particle x-position increases, mobilities decrease slowly (rapidly) near cavity center (wall). The decreasing trends for M_x and M_y (M_z) with x/h are different: the slowly decaying regions for M_y and M_z are wider than that for M_x. It is also observed that, near the wall, mobilities decrease more abruptly as R/h increases. On the second line, M_x (M_y) is perpendicular to the wall at $x = h (y = h)$ and $M_x = M_y$, while M_z is parallel to these walls. Observations on the first line for mobilities perpendicular and parallel to the wall also apply to those on the second line. One difference is that, as the particle on the second line is affected more greatly by the wall at $y = h$, M_z on the second line is smaller than that on the first line at the same x-position.

Based on symmetric properties of the cubic geometry, we speculate that particle mobilities in the entire cavity can be reduced to a minimal set in a subregion of the cavity. To find this subregion, we start by dividing the cubic cavity into eight subcubes using three midplanes at $x = 0$, $y = 0$, and $z = 0$. Mobilities in the entire cavity can then be determined by those in only one of the subcubes. We choose a representative subcube defined by the origin and its diagonal vertex (h, h, h) as shown in Fig. 1a. Next, we consider the diagonal plane of symmetry of the cubic cavity, and the chosen subcube can be further divided into two triangular prisms. A representative prism defined by (0, 0, 0), $(h, 0, 0)$, $(h, h, 0)$, (0, 0, h), $(h, 0, h)$, and (h, h, h) is chosen, and mobilities in the other prism can be calculated based on those in the chosen prism. Finally, by taking advantage of the commutative property of mobilities in the cubic cavity, the chosen prism can be divided into three tetrahedra. The commutative property is related to diagonal planes of symmetry, and one example is $M_x(a, b, c) = M_x(a, c, b) = M_y(b, a, c) = M_y(c, a, b) = M_z(b, c, a) = M_z(c, b, a)$ where a, b, and c are components of the particle center's coordinate. One representative tetrahedron defined by (0, 0, 0), (h, 0, 0), (h, 0, h), and (h, h, h) is marked out by yellow lines in Fig. 1a. We arrive at the minimal set formed by mobilities in one of the tetrahedra, which can be used to determine mobilities in the entire cavity.

We also analyze fluid velocities in the cavity induced by the particle motion. Three cases are considered: in the first, the particle is at the cavity center and the external force is along positive x-direction; in the second, the particle is at (0.5h, 0, 0) and the ex-

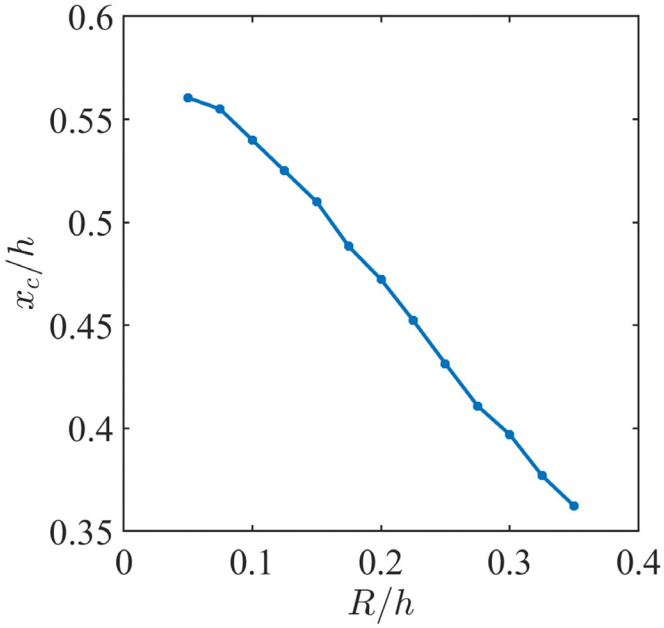

Fig. 5. Critical particle position x_c/h for vortex transition as a function of R/h. To determine x_c/h, the particle is placed on multiple locations along x-axis and an external force in y-direction is applied. When $0 \le x/h < x_c/h$, two vortices exist in the xy plane; when $x_c/h < x/h < 1$, only one vortex exits.

ternal force is the same as that in the first case; in the third, the particle location is the same as that in the second case while the external force is along positive y-direction. We choose a midplane of the cubic cavity at $z = 0$, and analyze fluid velocities in x- and y-directions (u and v) and streamlines in this plane. As shown in Fig. 4a, u is positive in the vicinity of the particle, but is negative near walls perpendicular to y-axis. From Fig. 4b, we can see that v is diagonally symmetric about the particle, with v being positive in the upper right and lower left regions of the plane and negative in the upper left and lower right regions. Fig. 4c shows streamlines, and two vortices are observed near the particle. The line connecting two stagnation points in the centers of vortices is found to be perpendicular to the applied force. In the second case, the overall pattern of fluid velocity distributions is similar to those in the first case as shown in Fig. 4d–f. Nonetheless, the distribution of negative u becomes more blunt near the wall at $x = h$ in the second case; v is no longer diagonally symmetric about the particle, and its distribution near the wall becomes elongated along y-direction compared to that in the first case. Fig. 4g–i show results in the third case. As the particle is near the wall and the force direction changes, the overall flow pattern becomes different from those in previous cases. The maximal magnitude of u on the left of the particle is larger than that on the right; the region of nonzero fluid velocity on the left is wider than that on the right. v is positive near the particle, but is negative near the wall on the left of the particle. From the streamlines, only one vortex is observed on the left of the particle.

To determine the critical particle position x_c/h for the transition from two vortices to one vortex, we place the particle on multiple locations along x-axis and apply an external force in y-direction. By counting the number of vortices in the xy plane for each simulation, it is found that x_c/h decreases with increasing R/h as shown in Fig. 5. This is because the no-slip wall nearest to the particle exerts greater influence on the particle with higher R/h, making the vortex between the particle and its nearest wall disappear at a smaller x_c/h.

Prior studies found that the particle will drift perpendicular to the external force because of the anisotropy of the mobility tensor induced by no-slip walls [28]. Here we study the drift motion of the spherical particle in a cubic cavity. The particle is placed in a plane defined by $0 \le x/h \le 1, y/h = 0.75$, and $0 \le z/h \le 1$. The external force along x-direction is applied on the particle, and the main velocity along x-direction (U_x) and drift velocity along y-direction (U_y) are measured. Fig. 6a shows two-dimensional distribution of the scaled drift velocity (U_y/U_x) in the plane. In general, the drift velocity near the wall at $x = h$ is larger than that near the cavity center. To examine the effect of confinement level on the drift velocity, we calculate variations of U_y/U_x, under various R/h, along a line defined by $0 \le x/h \le 1, y/h = -0.75$, and $z = 0$, and results are presented in Fig. 6b. We find that the scaled drift velocity at a certain x/h increases as R/h increases. For all R/h con-

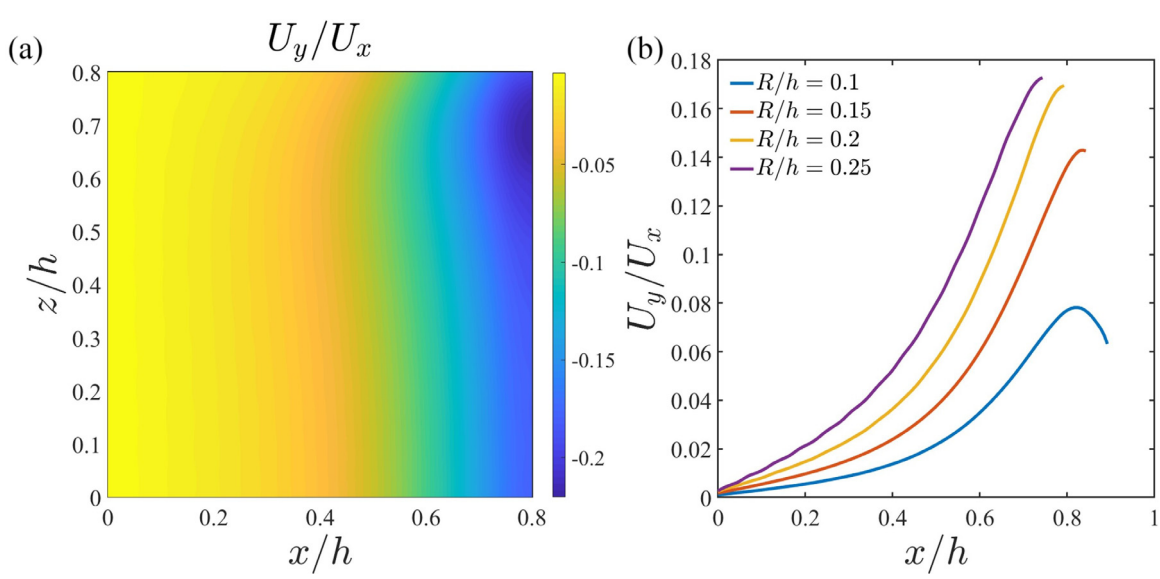

Fig. 6. (**a**) Two-dimensional distribution of normalized drift velocity along y-direction (U_y/U_x) for a particle with $R/h = 0.2$ in the plane defined by $0 \le x/h \le 1, y/h = 0.75$, and $0 \le z/h \le 1$. The external force is along x-direction. (**b**) Normalized drift velocity of a particle with $y/h = -0.75$ and $z = 0$ plotted against x/h for different R/h. (For interpretation of the references to color in this figure legend, the reader is referred to the web version of this article.)

sidered here, the increasing rate of the scaled drift velocity with x/h increases in the interior of the cavity, but decreases when the particle gets very close to the wall. For $R/h = 0.1$, the scaled drift velocity increases (decreases) when $x/h < 0.825$ ($x/h > 0.825$). As x/h increases and the particle moves further away from the symmetry plane (midplane at $z = 0$), the flow around the particle becomes more asymmetric with respect to the plane at $y/h = -0.75$. As a result, forces that the fluid exerts on the particle's two hemispheres along y-direction become more imbalanced, driving the magnitude of drift velocity up. On the other hand, as the particle moves closer to the wall, particle velocity tends to decreases due to the greater influence of the no-slip wall. Thus, the competition between effects of flow asymmetry and no-slip wall leads to the nonlinear variation of the drift velocity.

To conclude, we have studied hydrodynamic mobility and drift motion of a spherical particle in a low-Reynolds-number fluid confined by a cubic cavity using numerical simulations. Fluid velocities induced by the particle motion were also analyzed for different particle positions and external forces. We found that mobilities in the entire cavity can be computed based on a minimal set in a unit tetrahedron in the cavity. Fluid vortices in the cavity induced by the particle motion were analyzed. It was also found that the particle's drift velocity perpendicular to the external force depends on particle position and particle-to-cavity sizes ratio. This work forms the basis for understanding more complex particle dynamics under total confinement, which could benefit microfluidic applications such as intracellular transport and encapsulation technologies.

Declaration of Competing Interest

The authors declare that they have no known competing financial interests or personal relationships that could have appeared to influence the work reported in this paper.

Acknowledgments

This work was supported by the Young Elite Scientists Sponsorship Program by the Chinese Society of Theoretical and Applied Mechanics (CSTAM).

References

[1] J.K. Hamilton, A.D. Gilbert, P.G. Petrov, et al., Torque driven ferromagnetic swimmers, Phys. Fluids 30 (2018) 092001.
[2] G. Kabacaoglu, G. Biros, Sorting same-size red blood cells in deep deterministic lateral displacement devices, J. Fluid Mech. 859 (2019) 433.
[3] J. Happel, H. Brenner, Low Reynolds Number Hydrodynamics: with Special Applications to Particulate Media, Prentice-Hall, Inc., New Jersey, 1965.
[4] E. Gonzalez, C. Aponte-Rivera, R.N. Zia, Impact of polydispersity and confinement on diffusion in hydrodynamically interacting colloidal suspensions, J. Fluid Mech. 925 (2021) A35.
[5] J. Li, X. Jiang, A. Singh, et al., Structure and dynamics of h ydrodynamically interacting finite-size Brownian particles in a spherical cavity: spheres and cylinders, J. Chem. Phys. 152 (2020) 204109.
[6] A. Singh, J. Li, X. Jiang, et al., Shape induced segregation and anomalous particle transport under spherical confinement, Phys. Fluids 32 (2020) 053307.
[7] C. Aponte-Rivera, Y. Su, R.N. Zia, Equilibrium structure and diffusion in concentrated hydrodynamically interacting suspensions confined by a spherical cavity, J. Fluid Mech. 836 (2018) 413.
[8] C. Aponte-Rivera, R.N. Zia, Simulation of hydrodynamically interacting particles confined by a spherical cavity, Phys. Rev. Fluids 1 (2016) 023301.
[9] J. Skolnick, Perspective: on the importa nce of hydrodynamic interactions in the subcellular dynamics of macromolecules, J. Chem. Phys. 145 (2016) 100901.
[10] L. Xiang, K. Chen, R. Yan, et al., Single-molecule displacement mapping unveils nanoscale heterogeneities in intracellular diffusivity, Nat. Methods 17 (2020) 524.
[11] J.H. Khoo, H. Miller, J.P. Armitage, Measurement of macromolecular crow ding in *Rhodobac ter sphaeroides* under different growth conditions, mBio 13 (2022) e03672.
[12] J. van de Meent, A.J. Sederman, L.F. Gladden, et al., Measurement of cytoplasmic streaming in single plant cells by magnetic resonance velocimetry, J. Fluid Mech. 642 (2010) 5.
[13] R.E. Goldstein, I. Tuval, J. van de Meent, Microfluidics of cytoplasmic streaming and its implications for intracellular transport, Proc. Natl. Acad. Sci. USA 105 (2008) 3663.
[14] H. Wang, G. Hu, P granu les phase transition induced by cytoplasmic streaming in *Caenorhabditis elegans* embryo, Sci. China Phys. Mech. 60 (2017) 1.
[15] E. Chow, J. Skolnick, Effects of confinement on models of intracellular macromolecular dynamics, Proc. Natl. Acad. Sci. 112 (2015) 14846.
[16] A.E. Cervantes-Martinez, A. Ramirez-Saito, R. Armenta-Calderon, et al., Colloidal diffusion inside a spherical cell, Phys. Rev. E 83 (2011) 030402.
[17] H.J. Keh, T.C. Lee, Axisymmetric creeping motion of a slip spherical particle in a nonconcentric spherical cavity, Theor. Comput. Fluid Dyn. 24 (2010) 497.
[18] M.S. Faltas, E.I. Saad, Stokes flow past an assemblage of slip eccentric spherical particle-in-cell models, Math. Methods Appl. Sci. 34 (2011) 1594.
[19] T.C. Lee, H.J. Keh, Slow motion of a spherical particle in a spherical cavity with slip surfaces, Int. J. Eng. Sci. 69 (2013) 1.
[20] S. Koi, M. Kato, Comparative develo pmental anatomy of the root in three species of *Cladopus* (Podostemaceae), Ann. Bot. 91 (2003) 927.
[21] P.C. Dantas, J.E. Serrao, H.C.P. Santos, et al., Anatomy and histology of the alimentary canal of larvae and adults of *Chry soperla externa* (Hagen, 1861) (Neuroptera: Chrysopidae), Arthropod Struct. Dev. 60 (2021) 101000.
[22] Y.E. Geints, Numerical study of photothermal effect in core-shell microcapsules, J. Quant. Spectrosc. Radiat. Transf. 255 (2020) 107266.
[23] L. Hedhili, A. Sellier, L. Elasmi, et al., Motion of small solid particles in a viscous fluid enclosed in a cavity, CMES - Comput. Model. Eng. Sci. 73 (2011) 137.
[24] X. Zhao, J. Li, X. Jiang, et al., Parallel O(N) Stokes' solve r towards scalable Brownian dynamics of hydrodynamically interacting objects in general geometries, J. Chem. Phys. 146 (2017) 244114.
[25] P. Pranay, S.G. Anekal, J.P. Hernandez-Ortiz, et al., Pair collisions of fluid -filled elastic capsules in shear flow: effects of membrane properties and polymer additives, Phys. Fluids 22 (2010) 123103.
[26] Y. Zhang, J.J.d. Pablo, M.D. Graham, An immersed boundary method for Brownian dynamics simulation of polymers in complex geometries: application to dna flowing through a nanoslit with embedded nanopits, J. Chem. Phys. 136 (2012) 014901.
[27] A. Kumar, R.G.H. Rivera, M.D. Graham, Flow-induced segregation in confined multicomponent suspensions: effects of particle size and rigidity, J. Fluid Mech. 738 (2014) 423.
[28] P. Ganatos, S. Weinbaum, R. Pfeffer, Gravitational and zero- drag motion of a sphere of arbitrary size in an inclined channel at low Reynolds number, J. Fluid Mech. 124 (1982) 27.